Journal of Computational Physics **183,** 1–25 (2002)
doi:10.1006/jcph.2002.7145

Numerical Investigation on the Stability of Singular Driven Cavity Flow

F. Auteri, N. Parolini, and L. Quartapelle

Dipartimento di Ingegneria Aerospaziale, Politecnico di Milano, Via La Masa 34, 20158 Milano, Italy
E-mail: auteri@aero.polimi.it

Received May 22, 2001; revised May 31, 2002

By applying the singularity subtraction technique to the unsteady driven cavity problem, the stability of the impulsively started flow is investigated, without smoothing the corner singularity. A second-order spectral projection method allows localization of the critical Reynolds number for the first Hopf bifurcation in the interval [8017.6, 8018.8). © 2002 Elsevier Science (USA)

Key Words: stability of incompressible viscous flows; unsteady driven cavity flows; critical Reynolds number; Hopf bifurcation.

1. INTRODUCTION

Classical studies on hydrodynamic stability usually concern problems with no-slip conditions on only one simple surface or two parallel surfaces, the prototype being Couette and Poiseuille flows. This class of studies allows a double simplification of the mathematical problem: the basic flow is known *analytically* and the eigenvalue problem for the stability analysis is an *ordinary differential* eigenvalue problem (see the classical monographs by Chandrasekhar [10] and Drazin and Reid [11]). By contrast, when the flow domain is characterized by two or three spatial directions with nonperiodic boundary conditions, the formulation of the stability problem requires solving a *partial differential* eigenvalue problem and, moreover, the basic steady flow can be determined in most cases only *numerically*.

In the particular case of incompressible flows, the analysis of the linear stability involves, for 2D plane flows, the solution of a biharmonic eigenvalue problem (see, e.g., [6]) and, for 3D flows periodic in one spatial direction, a system of two biharmonic equations coupled on the solid boundary (see, e.g., [27]). Another possibility is to write the eigenvalue problem for the coupled system of equations for the primitive variables velocity and pressure as done, for instance, in [12].

An alternative to the eigenvalue problem approach is the direct simulation of the flow, a method which allows exploration of the asymptotic character (steady, periodic,

0021-9991/02 $35.00

quasiperiodic, or other) of the solution depending on the value of the relevant parameters. This approach was employed, for example, by Gustafson and Halasi [18, 19] to study driven cavity flows by means of both a projection method based on a staggered-grid discretization and a time-dependent biharmonic formulation using standard finite differences.

However, the direct simulation is rather expensive in computer time since very long simulations are often needed—in particular when the flow parameters are near the critical values—so that the use of very efficient solvers is mandatory. On the other hand this approach presents the advantage of making the flow beyond the first Hopf bifurcation accessible.

Being interested in the stability of two-dimensional flows in confined domains, we developed a new spectral solver for the solution of the time-dependent Navier–Stokes equations formulated in primitive variables. The problem is discretized in time by means of a second-order projection scheme, which has provided the efficient algorithm described in [2]. The uncoupled solution procedure consists of a viscous step, where one problem for each velocity component is solved, and a projection step, where the incompressibility constraint is imposed. The second-order BDF approximation of the momentum equation allows us to follow the fluid dynamics with adequate accuracy. In the present paper, this spectral projection method is employed to solve the singular driven cavity problem in order to investigate the behavior of the flow as the Reynolds number increases.

The 2D flow in driven cavities has been extensively studied in the past 40 years, starting from the pioneering study of Kawaguti [21]. Since then, several works have contributed to establish a clear picture of the steady solutions to this problem for Reynolds numbers up to several thousand, mainly by employing vorticity–velocity and biharmonic solvers [13, 14, 30]. More recently, interest has focused on simulating the evolutionary problem and, in this context, on investigating the stability of the steady solution to determine the periodic solution through a Hopf bifurcation. These last investigations have been conducted on a rectangular cavity of aspect ratio 2 [15] and on a square cavity [28] under a suitable regularization of the singularity of the boundary condition. As originally defined by Burggraf, the driven cavity problem is characterized by rigid walls all around the flow domain. In this way, physically complicated inlet or outlet boundary conditions as well as unphysical periodic conditions are avoided, and the problem represents an ideal test case for investigations on the stability of the 2D flow inside a closed region.

The driven cavity problem presents however a well-known mathematical difficulty related to its boundary conditions. Indeed, the motion of the upper walls sliding on the fixed vertical walls makes the vorticity and the pressure singular in two corners of the cavity [17].

A method for overcoming this difficulty is to clean off the singular component of the solution by subtracting the analytically known singular solution from the unknown. This technique was applied for the first time to cavity flow by Schultz *et al.*, [31] who, working with the biharmonic equation for the streamfunction, subtracted only the first term of the singular solution of the Stokes problem (creeping flow). More recently the singularity subtraction scheme has been employed by Botella and Peyret in the primitive variable formulation [8] and by Auteri *et al.* in the vorticity–streamfunction uncoupled approach [4], by including the Stokes contribution as well as the first-order-in-Re term of the singularity.

This strategy is applied here to the time-dependent problem formulated in terms of the primitive variables to locate the stability limit of the stationary solution for the singular driven cavity problem in a square domain and to discover the nature of the periodic solution. Once the singularity has been subtracted, the problem can be discretized by means of

a spectral method and numerical solutions free from spatial oscillations due to Gibbs's phenomenon can be computed.

The paper is organized as follows. In Section 2 the singular driven cavity problem is defined by introducing the governing equations and the boundary conditions. In Section 3 the singularity subtraction technique is briefly sketched, the singular solution in the corner is recalled (Section 3.1), and the problem for the perturbation variables is defined (Section 3.2). Section 4 illustrates the second-order BDF projection method employed. Section 5 deals with the spatial discretization, introducing the bases adopted (Section 5.1) and the treatment of the nonlinear term (Section 5.2). In Section 6 the accuracy of the proposed numerical method is assessed, for both asymptotic steady solutions and oscillatory unsteady solutions. The results obtained in the localization of Hopf bifurcation are presented and discussed in Section 7. Section 8 is devoted to some concluding remarks.

The stability limit reported in this paper was communicated by the second author at the *Fourth Euromech Fluid Mechanics Conference* held in Eindhoven from the 19th to the 23th of November, 2000.

2. IMPULSIVELY STARTED DRIVEN CAVITY PROBLEM

We consider driven cavity flow governed by the incompressible Navier–Stokes equations, written in dimensionless form as

$$\begin{cases} \frac{\partial \boldsymbol{U}}{\partial t} - \frac{1}{\mathrm{Re}}\boldsymbol{\nabla}^2\boldsymbol{U} + (\boldsymbol{U}\cdot\boldsymbol{\nabla})\boldsymbol{U} + \boldsymbol{\nabla}P = 0, \\ \boldsymbol{\nabla}\cdot\boldsymbol{U} = 0, \\ \boldsymbol{U}_{|\partial\Omega} = \boldsymbol{A}, \\ \boldsymbol{U}_{|t=0} = \boldsymbol{U}_0 = 0. \end{cases} \tag{2.1}$$

The problem is defined in the square domain $\Omega = (0, 1)^2$ with the upper side of the cavity sliding to the left at unit velocity. Thus, the Dirichlet boundary datum A for the velocity is zero everywhere, except at $y = 1$, where $\boldsymbol{A} = -\hat{\boldsymbol{x}}$, with $\hat{\boldsymbol{x}}$ denoting the unit vector $(1, 0)$.

A well-known difficulty of this problem is the presence of singularities at the corners of the cavity. In particular, at the two upper corners A and B shown in Fig. 1, the pressure and

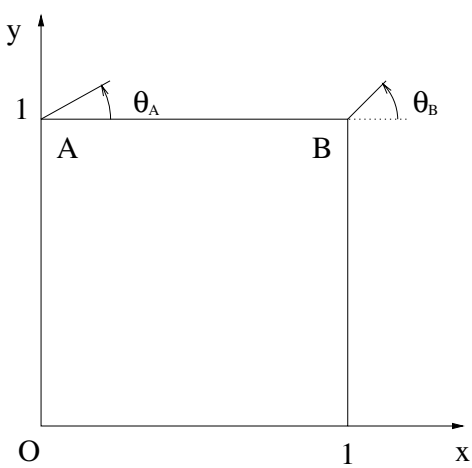

FIG. 1. Geometry of the driven cavity problem with its singular corners.

the vorticity are not finite, due to the discontinuity in the boundary datum for the horizontal velocity. The singularities at the two lower corners are much weaker (see, for instance, [8]) and therefore no specific treatment is adopted for them in the present work.

3. SUBTRACTION OF CORNER SINGULARITIES

3.1. Solution at Singular Corners

It is known that the steady bidimensional flow in the region sufficiently near a singular corner can be calculated analytically by considering the solution as an asymptotic expansion. In particular, the analysis of Batchelor [5] supplied the exact solution for creeping flow. Subsequently, Gupta *et al.* [17] and Hancock *et al.* [20] extended the analysis to a nonzero Reynolds number.

Let us first consider the singular flow near the top left corner A of coordinates (0, 1). We look for the solution of the following steady Navier–Stokes problem:

$$\begin{cases} -\frac{1}{\mathrm{Re}}\nabla^2\boldsymbol{u} + \nabla p + (\boldsymbol{u}\cdot\nabla)\boldsymbol{u} = 0, & \nabla\cdot\boldsymbol{u} = 0, \\ \boldsymbol{u}(x,1) = -\hat{\boldsymbol{x}},\ x > 0, & \boldsymbol{u}(0,y) = 0,\ y < 1. \end{cases} \tag{3.1}$$

The singular solution of (3.1) near the corner can be written by means of an asymptotic expansion. Here, we are interested only in the first two terms of the expansion, so that the truncated singular solution $(\boldsymbol{u}^A_{\mathrm{Re}}, p^A_{\mathrm{Re}})$ is defined by

$$\begin{cases} \boldsymbol{u}^A_{\mathrm{Re}} = \boldsymbol{u}^A_0 + \mathrm{Re}\,\boldsymbol{u}^A_{\mathrm{i}}, \\ p^A_{\mathrm{Re}} = \frac{p^A_0}{\mathrm{Re}} + p^A_{\mathrm{i}}, \end{cases} \tag{3.2}$$

with the subscript "i" denoting the "inertial" component of the singular solution. Notice that the zeroth-order term of the pressure is scaled with the Reynolds number due to the structure of the dimensionless Stokes problem.

The first component $(\boldsymbol{u}^A_0, p^A_0)$ of the expansion satisfies the following Stokes problem:

$$\begin{cases} -\nabla^2\boldsymbol{u}^A_0 + \nabla p^A_0 = 0, & \nabla\cdot\boldsymbol{u}^A_0 = 0, \\ \boldsymbol{u}^A_0(x,1) = -\hat{\boldsymbol{x}},\ x > 0, & \boldsymbol{u}^A_0(0,y) = 0,\ y < 1. \end{cases} \tag{3.3}$$

By virtue of problem (3.3) and neglecting the higher order terms, the second component (inertial) of the singular solution is found to be governed by the Stokes problem with a source term in the momentum equation (nonhomogeneous Stokes problem), namely,

$$\begin{cases} -\nabla^2\boldsymbol{u}^A_{\mathrm{i}} + \nabla p^A_{\mathrm{i}} = -\big(\boldsymbol{u}^A_0\cdot\nabla\big)\boldsymbol{u}^A_0, & \nabla\cdot\boldsymbol{u}^A_{\mathrm{i}} = 0, \\ \boldsymbol{u}^A_{\mathrm{i}}(x,1) = 0,\ x > 0, & \boldsymbol{u}^A_{\mathrm{i}}(0,y) = 0,\ y < 1. \end{cases} \tag{3.4}$$

Introducing a polar coordinate system (r,θ) centered in the corner A, so that the fluid is in the region with $-\pi/2 \le \theta \le 0$, the analytical solution of these two problems is obtained by means of variable separation [17, 20] (see also [8]). The solutions to problems (3.3) and (3.4) for the creeping flow component and the inertial component are given respectively by

$$\begin{cases} \boldsymbol{u}^A_0(\theta) = \boldsymbol{u}_0(\theta), \\ p^A_0(r,\theta) = \frac{p_0(\theta)}{r}, \end{cases} \quad \text{and} \quad \begin{cases} \boldsymbol{u}^A_{\mathrm{i}}(r,\theta) = r\boldsymbol{u}_{\mathrm{i}}(\theta), \\ p^A_{\mathrm{i}}(r,\theta) = (\ln r)\,p_{\mathrm{i}}. \end{cases}$$

For conciseness, we do not report the expressions for the functions $\boldsymbol{u}_0(\theta) = (u_0(\theta), v_0(\theta))$, $p_0(\theta)$, and $\boldsymbol{u}_{\mathrm{i}}(\theta)$ and the constant p_{i}, since they are all described in the references already cited.

The singular solution $\boldsymbol{u}^B$, p^B due to the discontinuity at the top right corner B is obtained similarly by considering a second polar system and the interval $\pi \le \theta \le 3\pi/2$. On account of the symmetry, the two components of the left corner singularity can also be easily obtained from their counterparts of the right corner and are found to be

$$\begin{cases} u^B_{\mathrm{Re}}(r,\theta) = u^B_0(\theta) + \ \mathrm{Re}\ u^B_{\mathrm{i}}(r,\theta) = u_0(\pi-\theta) - \ \mathrm{Re}\ r u_{\mathrm{i}}(\pi-\theta), \\ v^B_{\mathrm{Re}}(r,\theta) = v^B_0(\theta) + \ \mathrm{Re}\ v^B_{\mathrm{i}}(r,\theta) = -v_0(\pi-\theta) + \ \mathrm{Re}\ r v_{\mathrm{i}}(\pi-\theta), \\ p^B_{\mathrm{Re}}(r,\theta) = \frac{1}{\mathrm{Re}} p^B_0(r,\theta) + p^B_{\mathrm{i}}(r) = -\frac{1}{\mathrm{Re}} \frac{p_0(\pi-\theta)}{r} + (\ln r) p_{\mathrm{i}}. \end{cases}$$

The sums of the two singular contributions associated with the two upper corners are

$$\begin{cases} \boldsymbol{u}^S_{\mathrm{Re}} = \boldsymbol{u}^A_{\mathrm{Re}} + \boldsymbol{u}^B_{\mathrm{Re}} = \boldsymbol{u}^A_0 + \boldsymbol{u}^B_0 + \mathrm{Re}\big(\boldsymbol{u}^A_{\mathrm{i}} + \boldsymbol{u}^B_{\mathrm{i}}\big), \\ p^S_{\mathrm{Re}} = p^A_{\mathrm{Re}} + p^B_{\mathrm{Re}} = -\frac{1}{\mathrm{Re}}\big(p^A_0 + p^B_0\big) + p^A_{\mathrm{i}} + p^B_{\mathrm{i}}, \end{cases} \tag{3.5}$$

and, by virtue of problems (3.3) and (3.4), for $\mathrm{Re} > 0$ these satisfy the system

$$\begin{cases} -\frac{1}{\mathrm{Re}} \boldsymbol{\nabla}^2 \boldsymbol{u}^S_{\mathrm{Re}} + \boldsymbol{\nabla} p^S_{\mathrm{Re}} = -\big(\boldsymbol{u}^A_0 \cdot \boldsymbol{\nabla}\big)\boldsymbol{u}^A_0 - \big(\boldsymbol{u}^B_0 \cdot \boldsymbol{\nabla}\big)\boldsymbol{u}^B_0, \\ \boldsymbol{\nabla} \cdot \boldsymbol{u}^S_{\mathrm{Re}} = 0. \end{cases} \tag{3.6}$$

The values assumed by the singular solution $\boldsymbol{u}^S_{\mathrm{Re}}$ on the boundary of the original problem are

$$\begin{cases} \boldsymbol{u}^S_{\mathrm{Re}}(0, y) = \boldsymbol{u}^B_{\mathrm{Re}}(0, y), & 0 \le y \le 1, \\ \boldsymbol{u}^S_{\mathrm{Re}}(1, y) = \boldsymbol{u}^A_{\mathrm{Re}}(1, y), & 0 \le y \le 1, \\ \boldsymbol{u}^S_{\mathrm{Re}}(x, 0) = \boldsymbol{u}^A_{\mathrm{Re}}(x, 0) + \boldsymbol{u}^B_{\mathrm{Re}}(x, 0), & 0 \le x \le 1, \\ \boldsymbol{u}^S_{\mathrm{Re}}(x, 1) = -2\hat{\boldsymbol{x}}, & 0 \le x \le 1 \end{cases} \tag{3.7}$$

and are independent of time.

3.2. Problem for the Time-Dependent Perturbation

Since the solution corresponding to the corner singularities is known analytically, it can be subtracted from the unknowns of the original problem to obtain a problem for a perturbation. In the present case, the governing equations are the time-dependent Navier–Stokes equations while the singular solution corresponds to the steady problem and the application of the subtraction technique leads to an unsteady problem for the velocity and pressure perturbations. The procedure of subtracting the steady singular solution was found to be effective in the solution of the time-dependent vorticity and streamfunction equations [4]; this was also confirmed subsequently for primitive variable calculations by Botella and Peyret in [9]. Therefore it is quite natural to apply the same technique also in the time integration of the primitive-variable equations by means of the fractional step method.

To this aim, let us introduce the auxiliary unknowns u and p of the perturbation fields through the definitions

$$\begin{cases} \boldsymbol{U}(\boldsymbol{x}, t) = \boldsymbol{u}(\boldsymbol{x}, t) + \boldsymbol{u}^S_{\mathrm{Re}}(\boldsymbol{x}), \\ P(\boldsymbol{x}, t) = p(\boldsymbol{x}, t) + p^S_{\mathrm{Re}}(\boldsymbol{x}). \end{cases} \tag{3.8}$$

The singular contribution to the velocity solution is given by summing the zeroth-order and first-order components, namely,

$$\boldsymbol{u}^S_{\mathrm{Re}} = \boldsymbol{u}^S_0 + \mathrm{Re}\, \boldsymbol{u}^S_{\mathrm{i}}.$$

By substituting these expressions in the original Navier–Stokes problem (2.1) and considering Eqs. (3.5) and (3.6), a simple calculation leads to the following problem for the new unknowns $\boldsymbol{u}$ and p of the perturbation:

$$\begin{cases} \frac{\partial \boldsymbol{u}}{\partial t} - \frac{1}{\mathrm{Re}} \boldsymbol{\nabla}^2 \boldsymbol{u} + \boldsymbol{\nabla} p = -\big((\boldsymbol{u} + \boldsymbol{u}^S_{\mathrm{Re}}) \cdot \boldsymbol{\nabla}\big)(\boldsymbol{u} + \boldsymbol{u}^S_{\mathrm{Re}}) + (\boldsymbol{u}^A_0 \cdot \boldsymbol{\nabla})\boldsymbol{u}^A_0 + (\boldsymbol{u}^B_0 \cdot \boldsymbol{\nabla})\boldsymbol{u}^B_0, \\ \boldsymbol{\nabla} \cdot \boldsymbol{u} = 0, \\ \boldsymbol{u}_{|\partial\Omega} = \boldsymbol{a} = \boldsymbol{A} - \boldsymbol{u}^S_{\mathrm{Re}|\partial\Omega}, \\ \boldsymbol{u}_{|t=0} = -\boldsymbol{u}^S_{\mathrm{Re}}. \end{cases} \tag{3.9}$$

Thus, the singular subtraction technique leads to an incompressible problem similar to the original one, but for the nonlinear term which has a more complex structure and for the modified boundary and initial conditions. When only the Stokes singular contribution is considered, one has $\boldsymbol{u}^S_{\mathrm{Re}} \to \boldsymbol{u}^S_0 = \boldsymbol{u}^A_0 + \boldsymbol{u}^B_0$ and the last two terms involving $\boldsymbol{u}^A_0$ and $\boldsymbol{u}^B_0$ on the right-hand side of the momentum equation in (3.9) are absent. On the other hand, when the inertial contribution to the singular solution is retained, the two terms are present. They can be, however, eliminated by expanding the leading nonlinear term so that the most singular terms disappear from the momentum equation, thereby improving the accuracy. Thus, the nonlinear term will be given alternatively by the expressions

$$\begin{cases} \big((\boldsymbol{u} + \boldsymbol{u}^A_0 + \boldsymbol{u}^B_0) \cdot \boldsymbol{\nabla}\big)(\boldsymbol{u} + \boldsymbol{u}^A_0 + \boldsymbol{u}^B_0) & \text{if } \mathrm{Re} = 0, \\ \big((\boldsymbol{u} + \mathrm{Re}\, \boldsymbol{u}^S_{\mathrm{i}}) \cdot \boldsymbol{\nabla}\big)(\boldsymbol{u} + \boldsymbol{u}^S_{\mathrm{Re}}) + \big((\boldsymbol{u}^A_0 + \boldsymbol{u}^B_0) \cdot \boldsymbol{\nabla}\big)(\boldsymbol{u} + \mathrm{Re}\, \boldsymbol{u}^S_{\mathrm{i}}) & \\ \quad + (\boldsymbol{u}^A_0 \cdot \boldsymbol{\nabla})\boldsymbol{u}^B_0 + (\boldsymbol{u}^B_0 \cdot \boldsymbol{\nabla})\boldsymbol{u}^A_0 & \text{if } \mathrm{Re} > 0. \end{cases} \tag{3.10}$$

Notice that the perturbation velocity $\boldsymbol{u}$ satisfies boundary conditions independent of time obtained from the boundary datum $\boldsymbol{A}$ of the original problem and the (constant) boundary value of the singular solution $\boldsymbol{u}^S$. In particular, from (3.7), on the four sides the boundary datum $\boldsymbol{a}$ for $\boldsymbol{u}$ assumes the values

$$\begin{cases} \boldsymbol{a}(0, y) = \boldsymbol{a}^{\mathrm{left}}(y) = -\boldsymbol{u}^B_{\mathrm{Re}}(0, y), & 0 \le y \le 1, \\ \boldsymbol{a}(1, y) = \boldsymbol{a}^{\mathrm{right}}(y) = -\boldsymbol{u}^A_{\mathrm{Re}}(1, y), & 0 \le y \le 1, \\ \boldsymbol{a}(x, 0) = \boldsymbol{a}^{\mathrm{bottom}}(x) = -\boldsymbol{u}^S_{\mathrm{Re}}(x, 0) = -\boldsymbol{u}^A_{\mathrm{Re}}(x, 0) - \boldsymbol{u}^B_{\mathrm{Re}}(x, 0), & 0 \le x \le 1, \\ \boldsymbol{a}(x, 1) = \boldsymbol{a}^{\mathrm{top}}(x) = -\hat{\boldsymbol{x}} + 2\hat{\boldsymbol{x}} = \hat{\boldsymbol{x}}, & 0 \le x \le 1. \end{cases} \tag{3.11}$$

We remark that the solution $\boldsymbol{u}^A_{\mathrm{Re}}$ (resp. $\boldsymbol{u}^B_{\mathrm{Re}}$) is continuous on the right (resp. left) vertical side, which is internal to the domain of the corresponding problem. Thus, on the vertical

sides the following limits are defined:

$$\begin{cases} \lim_{y\to 1} \boldsymbol{a}(1, y) = \lim_{y\to 1}\left[-\boldsymbol{u}^A_{\mathrm{Re}}(1, y)\right] = \hat{\boldsymbol{x}}, \\ \lim_{y\to 1} \boldsymbol{a}(0, y) = \lim_{y\to 1}\left[-\boldsymbol{u}^B_{\mathrm{Re}}(0, y)\right] = \hat{\boldsymbol{x}}. \end{cases} \tag{3.12}$$

These coincide with the value assumed by the velocity on the upper horizontal wall by the fourth equation of (3.11). This shows that the singularity subtraction technique leads to the formulation of a new problem with *continuous* Dirichlet data for the perturbation velocity $\boldsymbol{u}$ on the entire boundary.

4. SECOND-ORDER PROJECTION METHOD

The perturbation problem is solved by means of an incremental projection method based on the two-step second-order BDF scheme for the time integration of the momentum equation (for details see [2] and [16]). We describe here how the scheme is employed to solve the incompressible problem (3.9) for the perturbation unknowns.

The two-step BDF scheme requires knowing the solution at two time levels. Thus, for the first step it is necessary to resort to a one-step scheme, and here the Euler formula has been employed. Moreover, since an incremental projection method is used, an initial pressure field p^0 is needed in addition to the initial velocity $\boldsymbol{u}^0 = -\boldsymbol{u}^S_{\mathrm{Re}}$. By the definition (3.7) of the perturbation pressure we have $p^0 = P^0 - p^S_{\mathrm{Re}}$. On the other hand, since in the original Navier–Stokes problem (2.1) we have $\boldsymbol{U}_{|t=0} = \boldsymbol{U}_0 = 0$, the associated initial pressure field P^0 can be assumed to be uniform, say $P^0 = 0$. We notice that there is no instantaneous buildup of the pressure since the impulsive initial motion of the wall is purely tangential. As a consequence, the initial condition for the perturbation pressure is $p^0 = -p^S_{\mathrm{Re}}$.

As the first time step ($k = 0$), we employ the incremental projection scheme based on the two-level Euler time discretization to determine the first velocity $\boldsymbol{u}^1$ and pressure p^1. If we take into account that $\boldsymbol{u}^0 + \boldsymbol{u}^S_{\mathrm{Re}} = -\boldsymbol{u}^S_{\mathrm{Re}} + \boldsymbol{u}^S_{\mathrm{Re}} = 0$, the first viscous diffusion problem assumes the form

$$\begin{cases} \frac{\boldsymbol{u}^1 - \boldsymbol{u}^0}{\Delta t} - \frac{1}{\mathrm{Re}}\boldsymbol{\nabla}^2\boldsymbol{u}^1 = (\boldsymbol{u}^A_0 \cdot \boldsymbol{\nabla})\boldsymbol{u}^A_0 + (\boldsymbol{u}^B_0 \cdot \boldsymbol{\nabla})\boldsymbol{u}^B_0 - \boldsymbol{\nabla} p^0, \\ \boldsymbol{u}^1_{|\partial\Omega} = \boldsymbol{a}, \end{cases} \tag{4.1}$$

and the Poisson problem for the first pressure increment reads

$$\begin{cases} -\hat{\boldsymbol{\nabla}}^2(p^1 - p^0) = -(\Delta t)^{-1}\boldsymbol{\nabla} \cdot \boldsymbol{u}^1, \\ (\partial(p^1 - p^0)/\partial n)_{|\partial\Omega} = 0. \end{cases} \tag{4.2}$$

Then, for $k \geq 1$ we introduce the linearly extrapolated velocity $\boldsymbol{u}^{k+1}_* \equiv 2\boldsymbol{u}^k - \boldsymbol{u}^{k-1}$ to guarantee the second-order accuracy of the explicit approximation of the nonlinear term.

The diffusion step for $k \geq 1$ is obtained by applying the BDF scheme to the momentum equation and, for the case with the intertial component of the singularity included, the

corresponding problem is obtained in the following form:

$$\begin{cases} \frac{3\boldsymbol{u}^{k+1}-4\boldsymbol{u}^{k}+\boldsymbol{u}^{k-1}}{2\Delta t}-\frac{1}{\mathrm{Re}}\boldsymbol{\nabla}^2\boldsymbol{u}^{k+1} \\ \quad =-\big(\big(\boldsymbol{u}_*^{k+1}+\mathrm{Re}\,\boldsymbol{u}_{\mathrm{i}}^{S}\big)\cdot\boldsymbol{\nabla}\big)\big(\boldsymbol{u}_*^{k+1}+\boldsymbol{u}_{\mathrm{Re}}^{S}\big) \\ \qquad -\big(\big(\boldsymbol{u}_0^{A}+\boldsymbol{u}_0^{B}\big)\cdot\boldsymbol{\nabla}\big)\big(\boldsymbol{u}_*^{k+1}+\mathrm{Re}\,\boldsymbol{u}_{\mathrm{i}}^{S}\big) \\ \qquad -\big(\boldsymbol{u}_0^{A}\cdot\boldsymbol{\nabla}\big)\boldsymbol{u}_0^{B}-\big(\boldsymbol{u}_0^{B}\cdot\boldsymbol{\nabla}\big)\boldsymbol{u}_0^{A} \\ \qquad -\begin{cases} \boldsymbol{\nabla}(3p^1-2p^0) & \text{for } k=1 \\ \frac{1}{6}\boldsymbol{\nabla}(14p^2-11p^1+3p^0) & \text{for } k=2 \\ \frac{1}{3}\boldsymbol{\nabla}(7p^k-5p^{k-1}+p^{k-2}) & \text{for } k\geq 3, \end{cases} \\ u_{|\partial\Omega}^{k+1}=\boldsymbol{a}. \end{cases} \tag{4.3}$$

Then, the projection step is performed through the following Neumann problem for the pressure increment $(p^{k+1}-p^k)$:

$$\begin{cases} -\hat{\boldsymbol{\nabla}}^2(p^{k+1}-p^k)=-\frac{3}{2\Delta t}\boldsymbol{\nabla}\cdot\boldsymbol{u}^{k+1}, \\ (\partial(p^{k+1}-p^k)/\partial n)_{|\partial\Omega}=0. \end{cases} \tag{4.4}$$

Note the different expressions for the "extrapolated" pressure in (4.3) at the two steps with $k=1$ and $k=2$. They result from the elimination of the first end-of-step velocity provided by the relation $u^1-\Delta t\hat{\boldsymbol{\nabla}}(p^1-p^0)$, which is at the origin of the Poisson equation in (4.2).

5. SPATIAL APPROXIMATION BY GALERKIN–LEGENDRE SPECTRAL METHOD

5.1. Fully Discrete Equations

We introduce the finite dimensional space $\boldsymbol{X}_N=(\mathbb{P}_N\otimes\mathbb{P}_N)^2$ for the approximation of the velocity and the space $Q_{\hat{N}}=\mathbb{P}_{\hat{N}}\otimes\mathbb{P}_{\hat{N}}$ for the approximation of the pressure. The polynomial order N for the velocity is in general different from the polynomial order $\hat{N}$ for the pressure; in particular we will consider $N=\hat{N}+2$ to satisfy the compatibility *inf–sup* condition (see, e.g., [7]). To recast (4.3) in a weak form by the Galerkin–Legendre spectral method, we consider two different bases for approximating velocity and pressure.

Since the velocity field is subjected to Dirichlet conditions, we adopt the basis introduced by Shen denoed by $L_n^*(x)$, for $n=0,\,1,\,2,\ldots$; for details see [29] and [3]. This basis includes the first two modes for imposing nonhomogeneous boundary values by means of a (numerical) lifting described in [3], where the matrix profiles and elements of the stiffness and mass matrices are also provided.

As far as the pressure approximation is concerned, the choice of the polynomial basis depends on whether the projection step is formulated as a Darcy problem or as a Poisson equation. In the present spectral projection method the pressure satisfies a Neumann boundary value problem, and the natural basis for the two-dimensional problem is simply the direct product of the standard Legendre polynomials normalized so as to obtain a mass matrix coincident with the identity matrix: $L_{\hat{n}}^{\diamond}(x)=\sqrt{\hat{n}+1/2}\,L_{\hat{n}}(x)$ for $\hat{n}=0,\,1,\,2,\ldots$ For a detailed analysis of the proper choice of the order of the polynomial basis for pressure and velocity see [1].

These two bases both refer to the interval $[-1,\,1]$ and therefore the transformation $x\to(2x-1)$ is required to match with the unit interval $[0,\,1]$ of the considered cavity. The

velocity and pressure fields, solution to the fractional step equations (4.3) and (4.4) [(4.1) and (4.2) for the first step], are expanded in the double series as

$$\boldsymbol{u}_N^{k+1}(x, y) = \sum_{n=0}^{N}\sum_{m=0}^{N} \boldsymbol{U}_{n,m}^{k+1} L_n^*(2x-1) L_m^*(2y-1), \tag{5.1}$$

$$p_{\hat{N}}^{k+1}(x, y) = \sum_{\hat{n}=0}^{\hat{N}}\sum_{\hat{m}=0}^{\hat{N}} P_{\hat{n},\hat{m}}^{k+1} L_{\hat{n}}^{\diamond}(2x-1) L_{\hat{m}}^{\diamond}(2y-1), \tag{5.2}$$

The capital letters $\boldsymbol{U}$ and P denote the arrays of the expansion coefficients and are not to be confused with the unknowns of the original Navier–Stokes problem (2.1).

The fully discrete momentum equations in weak form are given by the Galerkin method and read, for the general viscous step with $k \geq 3$, as follows.

For $k \geq 3$, find $\boldsymbol{u}_N^{k+1} \in \boldsymbol{X}_N$, with $\boldsymbol{u}_N^{k+1}|_{\partial\Omega} = \boldsymbol{a}$, such that, for all $\boldsymbol{v}_N \in \boldsymbol{X}_{0,N} = \boldsymbol{X}_N \cap \boldsymbol{H}_0^1(\Omega)$,

$$\begin{aligned}
&\left(\boldsymbol{v}_N, \frac{3\boldsymbol{u}_N^{k+1} - 4\boldsymbol{u}_N^{k} + \boldsymbol{u}_N^{k-1}}{2\Delta t}\right) + \frac{1}{\mathrm{Re}}\left(\boldsymbol{\nabla}\boldsymbol{v}_N, \boldsymbol{\nabla}\boldsymbol{u}_N^{k+1}\right) \\
&\quad = -\left(\boldsymbol{v}_N, \left(\left(\boldsymbol{u}_{N,*}^{k+1} + \mathrm{Re}\,\boldsymbol{u}_{\mathrm{i}}^{S}\right)\cdot\boldsymbol{\nabla}\right)\left(\boldsymbol{u}_{N,*}^{k+1} + \boldsymbol{u}_{\mathrm{Re}}^{S}\right)\right)_N \\
&\qquad - \left(\boldsymbol{v}_N, \left(\left(\boldsymbol{u}_0^{A} + \boldsymbol{u}_0^{B}\right)\cdot\boldsymbol{\nabla}\right)\left(\boldsymbol{u}_{N,*}^{k+1} + \mathrm{Re}\,\boldsymbol{u}_{\mathrm{i}}^{S}\right)\right)_N \\
&\qquad - \left(\boldsymbol{v}_N, \left(\boldsymbol{u}_0^{A}\cdot\boldsymbol{\nabla}\right)\boldsymbol{u}_0^{B} + \left(\boldsymbol{u}_0^{B}\cdot\boldsymbol{\nabla}\right)\boldsymbol{u}_0^{A}\right)_N \\
&\qquad - \frac{1}{3}\left(\boldsymbol{v}_N, \boldsymbol{\nabla}\left(7p_{\hat{N}}^{k} - 5p_{\hat{N}}^{k-1} + p_{\hat{N}}^{k-2}\right)\right),
\end{aligned} \tag{5.3}$$

where the discrete counterpart of the inner product has been defined by means of the Gauss–Legendre quadrature, namely,

$$\begin{aligned}
&\left(L_n^*(2x-1)L_m^*(2y-1),\, f(x, y)\right)_N \\
&\quad = \sum_{h=1}^{\frac{3}{2}(N+1)}\sum_{k=1}^{\frac{3}{2}(N+1)} L_n^*(2x_h-1)L_m^*(2y_k-1) f(x_h, y_k) w_h\, w_k,
\end{aligned} \tag{5.4}$$

with x_h and w_h denoting the Gauss–Legendre integration (mapped) points and weights. The number of points in the quadrature rule has been selected to avoid aliasing errors, which could produce numerical instabilities at high Reynolds numbers [2].

Choosing $\boldsymbol{X}_N + \hat{\boldsymbol{\nabla}} Q_{\hat{N}}$ as the functional space for the end-of-step velocity, we find that the weak form of the projection step of the BDF method reads:

For $k \geq 1$, find $(p_{\hat{N}}^{k+1} - p_{\hat{N}}^{k}) \in Q_{\hat{N}}$ such that, for all $q_{\hat{N}} \in Q_{\hat{N}}$,

$$\left(\hat{\boldsymbol{\nabla}}_{q_{\hat{N}}}, \hat{\boldsymbol{\nabla}}\left(p_{\hat{N}}^{k+1} - p_{\hat{N}}^{k}\right)\right) = -\frac{3}{2\Delta t}\left(q_{\hat{N}}, \boldsymbol{\nabla}\cdot\boldsymbol{u}_N^{k+1}\right). \tag{5.5}$$

5.2. Evaluation of the Nonlinear Term

As already stated, the singularity subtraction technique leads to a new incompressible problem with the momentum equation different from the original one only for the nonlinear term. The corresponding term in the weak equation can be evaluated by means of numerical quadrature based on Gauss–Legendre integration points, as done in the solver for the standard Navier–Stokes problem [2].

For the sake of simplicity, we first consider the nonlinear term of the momentum equation obtained by subtracting only the Stokes singular term. For the x component of the momentum equation, noticing that in this case the two last nonlinear terms on the right hand of the momentum equation in (5.3) are absent, we have the term $((\boldsymbol{u}_N + \boldsymbol{u}_0^S)\cdot\boldsymbol{\nabla})(u_N + u_0^S)$, which in weak form yields the matrix elements

$$C_{n,m} = \big(L_n^*(2x-1)L_m^*(2y-1),\ \big((\boldsymbol{u}_N + \boldsymbol{u}_0^S)\cdot\boldsymbol{\nabla}\big)\big(u_N + u_0^S\big)\big)_N,$$

where $\boldsymbol{u}_0^S = \boldsymbol{u}_0^A + \boldsymbol{u}_0^B$. To determine the values $C_{n,m}$, one first introduces the point values of the perturbation $\boldsymbol{u}_N = (u_N, v_N)$ at the $\frac{3}{2}(N+1)\times\frac{3}{2}(N+1)$ Gauss–Legendre points in the square $[-1,1]^2$,[1]

$$\boldsymbol{u}_N(x,y) \to \boldsymbol{\mathcal{U}} \equiv \left\{\boldsymbol{u}_N(x_h, y_k),\ 1 \le (h,k) \le \frac{3}{2}(N+1)\right\},$$

where $\boldsymbol{\mathcal{U}} = (\mathcal{U}, \mathcal{V})$ and, similarly, the point values of the derivatives of $\boldsymbol{u}_N$ at the Gauss–Legendre integration points,

$$\boldsymbol{\mathcal{U}}_{(x)} \equiv \left\{\frac{\partial \boldsymbol{u}_N(x_h, y_k)}{\partial x},\ 1 \le (h,k) \le \frac{3}{2}(N+1)\right\},$$
$$\boldsymbol{\mathcal{U}}_{(y)} \equiv \left\{\frac{\partial \boldsymbol{u}_N(x_h, y_k)}{\partial y},\ 1 \le (h,k) \le \frac{3}{2}(N+1)\right\}.$$

All these point values can be evaluated from the Legendre coefficient arrays $\boldsymbol{U} = (U, V)$ by means of

$$\boldsymbol{\mathcal{U}} = \mathcal{L}^*\boldsymbol{U}\mathcal{L}^{*T},\quad \boldsymbol{\mathcal{U}}_{(x)} = \mathcal{L}^{*\prime}\boldsymbol{U}\mathcal{L}^{*T},\quad \boldsymbol{\mathcal{U}}_{(y)} = \mathcal{L}^*\boldsymbol{U}\mathcal{L}^{*\prime T},$$

where we have introduced the (rectangular) matrices containing the values of the basis functions and of their derivatives at the same Gauss–Legendre points:

$$\mathcal{L}^* \equiv \left\{\mathcal{L}^*_{h,n} = L_n^*(2x_h - 1),\ 1 \le h \le \frac{3}{2}(N+1),\quad 0 \le n \le N\right\},$$
$$\mathcal{L}^{*\prime} \equiv \left\{\mathcal{L}^{*\prime}_{h,n} = dL_n^*(2x_h - 1)/dx,\ 1 \le h \le \frac{3}{2}(N+1),\quad 0 \le n \le N\right\}.$$

The matrix of point values of the Stokes singular component is defined similarly by

$$\boldsymbol{u}_0^S(x,y) \to \boldsymbol{\mathcal{U}}_0^S \equiv \left\{\boldsymbol{u}_0^S(x_h, y_k),\ 1 \le (h,k) \le \frac{3}{2}(N+1)\right\},$$

with analogous expressions for its derivatives. Since the singular solution component is constant in time, the corresponding matrices can be computed once and for all.

The array $\mathcal{C} = \{\mathcal{C}_{h,k}, 1 \le (h,k) \le \frac{3}{2}(N+1)\}$ of the point values of the nonlinear term $((\boldsymbol{u}_N + \boldsymbol{u}_0^S)\cdot\boldsymbol{\nabla})(u_N + u_0^S)$ is obtained from the relation

$$\mathcal{C} = \big(\mathcal{U} + \mathcal{U}_0^S\big) \,\dot{\star}\, \big[\mathcal{U}_{(x)} + \mathcal{U}_{0\,(x)}^S\big] + \big(\mathcal{V} + \mathcal{V}_0^S\big) \,\dot{\star}\, \big[\mathcal{U}_{(y)} + \mathcal{U}_{0\,(y)}^S\big],$$

[1] Calligraphic capital letters are used hereafter to indicate arrays of quantities evaluated at the Gauss–Legendre integration points.

where ☆ denotes the element-by-element multiplication of matrices. The contribution of the nonlinear term to the weak momentum equation is evaluated by means of the direct-product Gauss–Legendre quadrature formula with $\frac{3}{2}(N+1) \times \frac{3}{2}(N+1)$ points, as provided by the definition (5.4) of the discrete approximation of the inner product. The sought for matrix $C = \{C_{n,m}\}$ of the L^2 projection of the nonlinear term is finally given by

$$C = \mathcal{L}^{*T} \mathcal{W} \mathcal{C} \mathcal{W} \mathcal{L}^*,$$

where the Gauss–Legendre weights have been framed in the diagonal matrix $\mathcal{W} = \text{diag}\,(w_1, w_2, \ldots, w_{\frac{3}{2}(N+1)})$. The nonlinear term $((\boldsymbol{u}_N + \boldsymbol{u}_0^S) \cdot \boldsymbol{\nabla})(v_N + v_0^S)$ for the y component of the momentum equation is evaluated by the same procedure. Notice that the evaluation of the nonlinear terms by Gauss–Legendre numerical quadrature is much in the same spirit of Orszag's old pseudo-spectral method [25]. In fact, it requires at each time step transforming from the space of the Legendre coefficients to the physical space of the integration points.

When the inertial component is retained in the singularity subtraction scheme, the complete nonlinear term of the momentum equation in (5.3), expressed in the weak formulation, yields the vector array

$$\begin{aligned} \boldsymbol{C}_{n,m} = \big(L_n^*(2x-1)L_m^*(2y-1),\ \big((\boldsymbol{u}_N + \operatorname{Re} \boldsymbol{u}_i^S) \cdot \boldsymbol{\nabla}\big)\big(\boldsymbol{u}_N + \boldsymbol{u}_{\text{Re}}^S\big) \\ + \big(\boldsymbol{u}_0^S \cdot \boldsymbol{\nabla}\big)\big(\boldsymbol{u}_N + \operatorname{Re} \boldsymbol{u}_{\text{i}}^S\big) + \big(\boldsymbol{u}_0^A \cdot \boldsymbol{\nabla}\big)\boldsymbol{u}_0^B + \big(\boldsymbol{u}_0^B \cdot \boldsymbol{\nabla}\big)\boldsymbol{u}_0^A\big)_N. \end{aligned}$$

Thus, the matrix of the coefficients $\boldsymbol{C}_{n,m}$ is still obtained from the matrix relation $\boldsymbol{C} = \mathcal{L}^{*T} \mathcal{W}\, \boldsymbol{\mathcal{C}} \mathcal{W} \mathcal{L}^*$, where $\boldsymbol{\mathcal{C}}$ is defined by

$$\begin{aligned} \boldsymbol{\mathcal{C}} = \big(\mathcal{U} + \operatorname{Re} \mathcal{U}_{\text{i}}^S\big) \☆ \big[\boldsymbol{\mathcal{U}}_{(x)} + \boldsymbol{\mathcal{U}}_{\text{Re}(x)}^S\big] + \big(\mathcal{V} + \operatorname{Re} \mathcal{V}_{\text{i}}^S\big) \☆ \big[\boldsymbol{\mathcal{U}}_{(y)} + \boldsymbol{\mathcal{U}}_{\text{Re}(y)}^S\big] \\ + \mathcal{U}_0^S \☆ \big[\boldsymbol{\mathcal{U}}_{(x)} + \operatorname{Re} \boldsymbol{\mathcal{U}}_{\text{i}(x)}^S\big] + \mathcal{V}_0^S \☆ \big[\boldsymbol{\mathcal{U}}_{(y)} + \operatorname{Re} \boldsymbol{\mathcal{U}}_{\text{i}(y)}^S\big] + \boldsymbol{\mathcal{C}}_0^{AB}, \end{aligned}$$

where

$$\boldsymbol{\mathcal{C}}_0^{AB} = \mathcal{U}_0^A \☆ \boldsymbol{\mathcal{U}}_{0(x)}^B + \mathcal{V}_0^A \☆ \boldsymbol{\mathcal{U}}_{0(y)}^B + \mathcal{U}_0^B \☆ \boldsymbol{\mathcal{U}}_{0(x)}^A + \mathcal{V}_0^B \☆ \boldsymbol{\mathcal{U}}_{0(y)}^A.$$

We notice that only the arrays $\boldsymbol{\mathcal{U}}, \boldsymbol{\mathcal{U}}_{(x)}$, and $\boldsymbol{\mathcal{U}}_{(y)}$ change at each time step, while all the remaining arrays can be evaluated once and for all at the beginning of the computations.

The algebraic problem obtained from the fully discrete equations requires solving, for each time step, two Helmholtz–Dirichlet problems for the velocity components and one Poisson–Neumann problem for the pressure. This has been done by employing two different direct elliptic solvers. The solver for the velocity components was based on the eigen-decomposition of the mass matrices in the two spatial directions (see [3]) while the solver for the pressure system was based on the eigen-decomposition of the stiffness matrices. A detailed and complete description of the BDF spectral projection method is provided in [2].

6. ACCURACY EVALUATION

The accuracy of the method described has been tested by solving the singular driven cavity problem at different Reynolds numbers. The result are compared with benchmark solutions obtained by Botella and Peyret [8] by means of a projection method based on a Chebyshev collocation technique. We consider the behavior of the solver against both steady solutions (Section 6.1) and unsteady ones (Section 6.2).

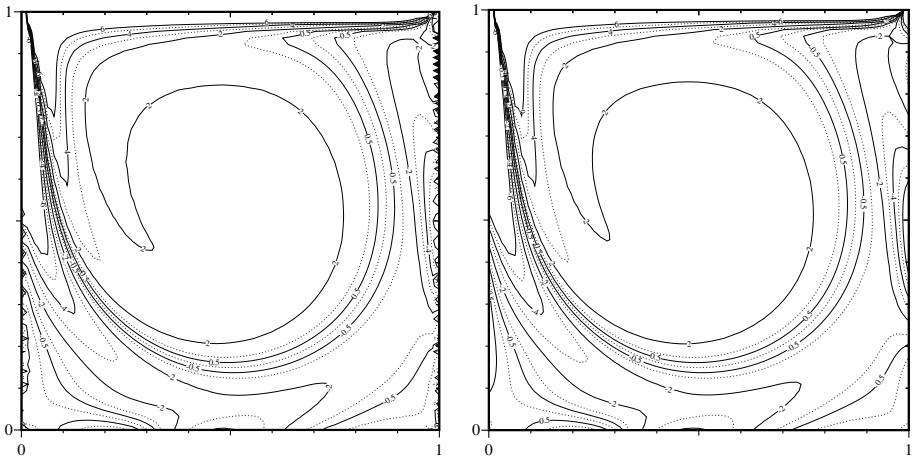

FIG. 2. Vorticity field for the steady flow in the cavity with $\mathrm{Re} = 1000$. Solution computed by the BDF spectral projection method with $\mathbb{P}_{64}$–$\mathbb{P}_{62}$ with no treatment for the singularity (left) and by substracting the singularity.

6.1. Steady Solutions

The first test has been performed for $\mathrm{Re} = 1000$. Figure 2 presents the vorticity levels of the steady-state solution using polynomials $\mathbb{P}_{64}$–$\mathbb{P}_{62}$ and a time step $\Delta t = 0.001$, obtained without subtracting the singularity (left) and by subtracting it (right). This comparison demonstrates the importance of the singularity subtraction technique in obtaining a spectral solution free from Gibbs spatial oscillations (see also [4]).

Some numerical comparisons with the benchmark solutions [8] for $\mathrm{Re} = 1000$ are reported in Tables I, II, and III. In particular, Table I presents the extreme values of the velocity through the centerlines of the cavity, while Tables II and III contain some local value of velocity and vorticity through the centerlines in the same points considered in [13] and [8].

TABLE I
Extrema of the Velocity through the Centerlines of the Cavity with Re = 1000

	N	$u_{\max}$	$y_{\max}$	$v_{\max}$	$x_{\max}$	$v_{\min}$	$x_{\min}$
Present	16	0.38811 97	0.1719	0.38221 98	0.8477	−0.52067 36	0.0947
	24	0.38838 83	0.1717	0.37675 61	0.8419	−0.52698 44	0.0906
	32	0.38854 23	0.1717	0.37691 06	0.8421	−0.52705 57	0.0908
	48	0.38857 16	0.1717	0.37694 16	0.8422	−0.52707 59	0.0908
	64	0.38857 03	0.1717	0.37694 33	0.8422	−0.52707 63	0.0908
	96	0.38856 97	0.1717	0.37694 47	0.8422	−0.52707 70	0.0908
	128	0.38856 98	0.1717	0.37694 47	0.8422	−0.52707 72	0.0908
	160	0.38856 98	0.1717	0.37694 47	0.8422	−0.52707 72	0.0908
Ref. [8]	48	0.38852 71	0.1717	0.37689 91	0.8422	−0.52701 68	0.0908
	64	0.38856 95	0.1717	0.37694 39	0.8422	−0.52707 63	0.0908
	96	0.38856 98	0.1717	0.37694 47	0.8422	−0.52707 71	0.0908
	128	0.38856 98	0.1717	0.37694 47	0.8422	−0.52707 71	0.0908
	160	0.38856 98	0.1717	0.37694 47	0.8422	−0.52707 71	0.0908

TABLE II
Vertical Velocity and Vorticity Values through the Horizontal Centerline of the Cavity with Re = 1000, $N = 160$

x	v, Ref. [8]	v	ω, Ref. [8]	ω
0.0000	0.00000 00	0.00000 00	−5.46217	−5.46120
0.0391	−0.29368 69	−0.29368 69	−8.24616	−8.24616
0.0547	−0.41037 54	−0.41037 54	−6.50867	−6.50866
0.1406	−0.42645 45	−0.42645 45	3.43016	3.43016
0.5000	0.02579 95	0.02579 95	2.06722	2.06722
0.7734	0.33399 24	0.33399 24	2.00174	2.00174
0.9062	0.33304 42	0.33304 43	−0.82398	−0.82398
0.9297	0.29627 03	0.29627 03	−1.50306	−1.50306
1.0000	0.00000 00	0.00000 00	−7.66369	−7.66289

TABLE III
Horizontal Velocity and Vorticity Values through the Vertical Centerline of the Cavity with Re = 1000, $N = 160$

y	u, Ref. [8]	u	ω, Ref. [8]	ω
1.0000	−1.00000 00	−1.00000 00	14.7534	14.7524
0.9688	−0.58083 59	−0.58083 60	9.49496	9.49496
0.9531	−0.47233 29	−0.47233 30	4.85754	4.85754
0.7344	−0.18867 47	−0.18867 47	2.09121	2.09121
0.5000	0.06205 61	0.06205 61	2.06722	2.06722
0.2813	0.28036 96	0.28036 96	2.26772	2.26772
0.1016	0.30045 61	0.30045 61	−1.63436	−1.63436
0.0625	0.20233 00	0.20233 00	−2.31786	−2.31786
0.0000	0.00000 00	0.00000 00	−4.16648	−4.16650

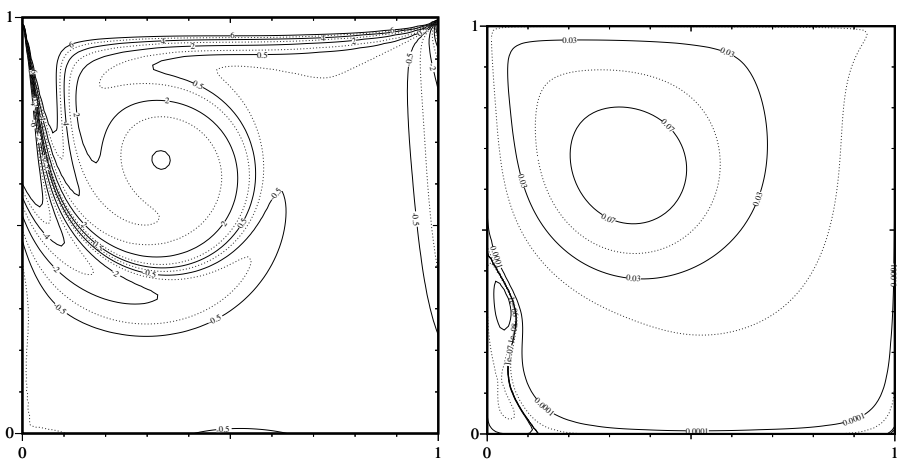

FIG. 3. Vorticity field and streamlines for the impulsively started driven cavity flow with Re = 1000 at $t = 6.25$. Solution computed by the BDF spectral projection method, using $\mathbb{P}_{96}$–$\mathbb{P}_{94}$ polynomials.

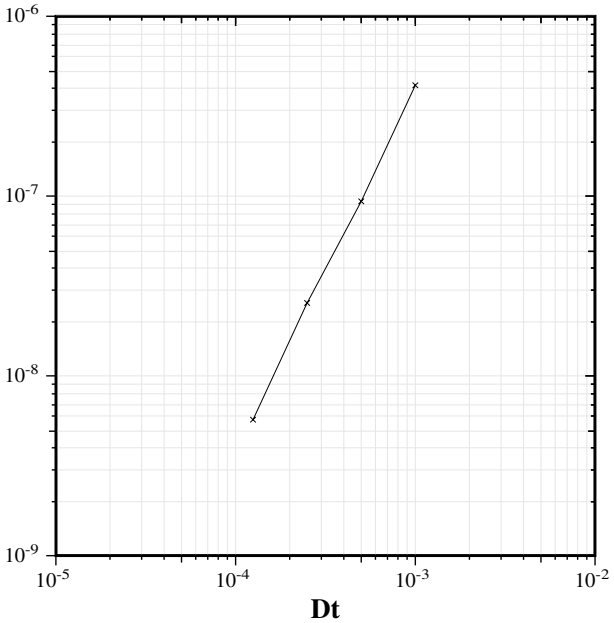

FIG. 4. Streamfunction value at the center of the cavity at $t = 6.25$ and $\mathrm{Re} = 1000$ for varying Δt. Differences between values computed by the second-order BDF spectral projection methods with $N = 96$ and $\hat{N} = 94$ and by the reference values provided by an $\mathcal{O}((\Delta t)^2)$-accurate spectral biharmonic solver with $N = 96$.

6.2. Unsteady Solutions

We now consider the behavior of the solver during the transient due to the impulsive start of the upper wall of the cavity. Figure 3 shows the solution at time $t = 6.25$, with $\mathrm{Re} = 1000$. The secondary eddy developing on the vertical wall shown in Fig. 3 is identical in shape and intensity to that obtained by a spectral biharmonic solver based on the Glowinski–Pironneau method [3].

To further assess the time accuracy of the solver against unsteady solutions, we compare the point value of the streamfunction in the center of the cavity computed with the proposed projection method with the value obtained by the vorticity–streamfunction solver with the second-order BDF time integration we have implemented (see Fig. 4). The second-order slope of the error curve indicates that the employed projection scheme achieves a true $\mathcal{O}((\Delta t)^2)$ accuracy. A more detailed account of the order of accuracy for velocity and pressure, in the relevant norms, of the proposed spectral projection method is provided in [1].

7. HOPF BIFURCATION IN THE SINGULAR DRIVEN CAVITY

The stability study of singular driven cavity flow is undertaken here by means of a direct simulation approach. Namely, several long-time simulations at different Reynolds numbers have been carried out to determine the asymptotic solutions of the problem for increasing Re. For the numerical computations we employed a Digital Alpha 433*au* workstation, using double-precision arithmetic to guarantee the necessary accuracy. In the simulations with various values of Re, we used the bases $\mathbb{P}_{64}$–$\mathbb{P}_{62}$. The BDF time integration scheme used in

the work is implicit for the viscous term while it relies upon a fully explicit extrapolation of the nonlinear terms. Due to such a treatment, a time-step limitation for numerical stability has been encountered in the simulations. The tests performed have shown that the step sizes guaranteeing numerical stability also provide solutions with the required accuracy. A rule of thumb adequate for this purpose has been determined experimentally to be the relation $\Delta t = 10/\mathrm{Re}$, for the Reynolds numbers and adopted spatial resolutions considered here.

7.1. Dynamic Indicator

In the analysis of unsteady cavity flows, the choice of the indicators suitable for monitoring the evolution of the system toward an asymptotic solution represents a critical aspect. Goodrich *et al.* [15] and Shen [28] employed the total kinetic energy as an indicator of the dynamics of the system. As pointed out in [15], different numerical experiments have shown that significant variations of the flow can still occur after the fluctuations of velocity have decreased to values smaller than 10^{-8}. As a consequence, to ensure that a true asymptotic state has been reached, the greatest attention must be paid to the choice of the criterion to be adopted for stopping the simulation.

The dynamic indicator adopted in the simulations presented here is the total kinetic energy of the perturbation velocity with respect to the singular solution, namely,

$$E(t) = \int_\Omega |\boldsymbol{u}(x, y, t)|^2 \, dx \, dy = \int_\Omega \left|\boldsymbol{U}(x, y, t) - \boldsymbol{u}^S_{\mathrm{Re}}(x, y)\right|^2 dx \, dy.$$

This choice is suggested by the very nature of the solver, which has the nonsingular auxiliary variables $\boldsymbol{u}(x, y, t)$ and $p(x, y, t)$ as unknowns.

7.2. Bifurcation: Localization of the Critical Value of Re

To determine the value of the critical Reynolds number, we have first detected two values of Re, namely $\mathrm{Re} = 5000$ and $\mathrm{Re} = 10000$, for which the asymptotic solution is found to be steady and periodic, respectively. Then, this interval, assumed to include the first critical Reynolds number, has been reduced by bisection. In this way, the first critical value $\mathrm{Re}_{\mathrm{cr}}$ has been localized in the small interval [8017.6, 8018.8).

This result sharpens the estimate $\mathrm{Re}_{\mathrm{cr}} = 8000$ found by Fortin *et al.* [12], through a classical eigenvalue analysis of the linearized Navier–Stokes equations, by means of a finite element spatial discretization. This difference can be attributed to the absence of an adequate treatment of the corner singularities in [12].

As will be shown, the system evolves to its asymptotic state with a velocity which decreases as the Reynolds number approaches its critical value, namely, as the real part of the more unstable pair of eigenvalues goes to zero. Therefore, carrying the simulations to convergence with Re very close to $\mathrm{Re}_{\mathrm{cr}}$ would have been too expensive. In these simulations, to discover whether the asymptotic behavior is a steady state or a periodic solution, the evolution of the energy fluctuation has been analyzed. In Fig. 5, we present the function $E(t)$ for different values of Re. This figure points out that, for $\mathrm{Re} > \mathrm{Re}_{\mathrm{cr}}$, the instability begins to develop for $t \leq 2500$. This is even clearer from Fig. 6, where it can be noted that for $t \approx 2000$ the kinetic energy signal presents a "knee." Our study has revealed that, in the proximity of the first Hopf bifurcation, the behavior near this point is sufficient to determine

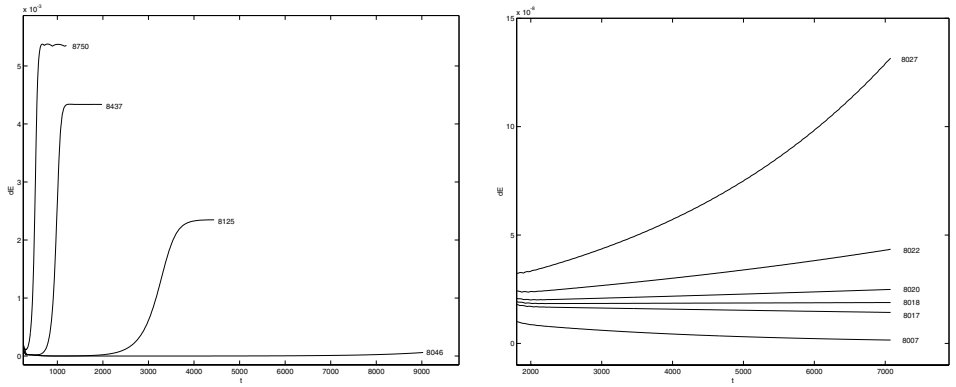

FIG. 5. Time evolution of the energy oscillation amplitude for different values of Re.

whether the asymptotic solution will be steady or not. In the steady case the oscillations present a maximum, corresponding to the knee (see the left plot of Fig. 6), while in the unsteady case the solution tends asymptotically to an oscillatory behavior (see the right plot of Fig. 6).

To verify whether a time step $\Delta t = 10/\mathrm{Re}$ is sufficiently small to guarantee the time accuracy, another simulation with $\mathrm{Re} = 8017.6$ has been carried out using a halved time step $\Delta t = 5/\mathrm{Re} = 0.00062$. Figure 7 compares the behavior of $E(t)$ using the two time steps. Both in the initial phase and for large t before reaching the steady asymptotic state, no appreciable difference is observed.

The accurate localization of the first Hopf bifurcation in the narrow interval [8017.6, 8018.8) has been confirmed by simulating the flows for the two bracketing values of Re, using a finer spatial resolution with polynomials $\mathbb{P}_{96}$–$\mathbb{P}_{94}$. Moreover, as a final check of the correctness of our estimate of $\mathrm{Re}_{\mathrm{cr}}$, we resorted to the vorticity–streamfunction formulation already considered in Section 6. The spectral solver for the ω–ψ equations is proposed in [3] and, for the present calculations, is combined with the singularity subtraction technique described in [4]. This solver enforces integral conditions on the vorticity by means of the spectral version of Glowinski–Pironneau method and has been implemented using the second-order-accurate BDF scheme for the vorticity transport equation. The results obtained

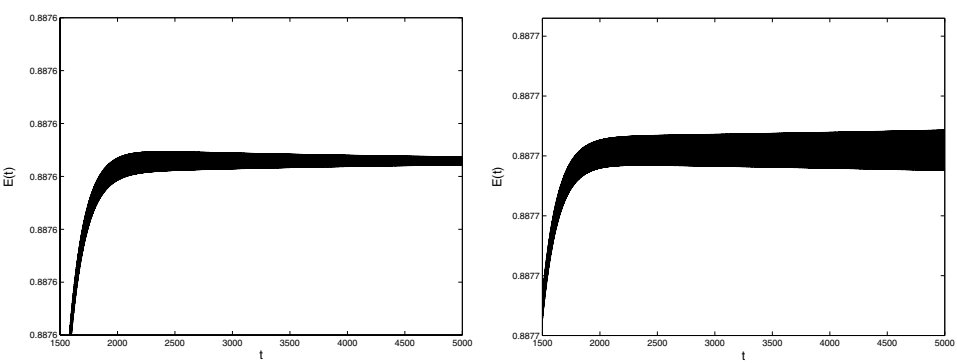

FIG. 6. Energy time series near $t = 2000$ for $\mathrm{Re} = 8007$ (left) and $\mathrm{Re} = 8022$ (right).

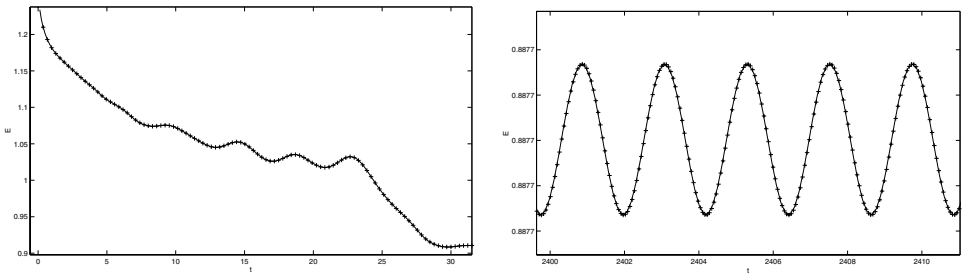

FIG. 7. Comparison between the time evolution of E for $\mathrm{Re} = 8017.6$ computed using $\Delta t = 0.00124$ (solid line) and $\Delta t = 0.00062(+)$.

by means of this completely different formulation, using the basis $\mathbb{P}_{96}$ for the two scalar unknowns, led to the same estimate of the interval containing $\mathrm{Re}_{\mathrm{cr}}$. The advantage of the present primitive variable method over the ω–ψ approach is that the former can be extended easily to the 3D equations.

7.3. Steady Solutions

The simulations with $\mathrm{Re} < \mathrm{Re}_{\mathrm{cr}}$ lead to steady asymptotic solutions. In Fig. 8, we report the steady streamlines for $\mathrm{Re} = 6125$, $\mathrm{Re} = 7500$, and $\mathrm{Re} = 7812.5$. These three fields display the same qualitative behavior. In particular, one observes a primary vortex in the center of the cavity, secondary vortices near the two lower corners and the right upper corner, and, finally, a tertiary vortex in the left lower corner. Figure 8 shows that, as the Reynolds number increases, the tertiary vortex grows and, for $\mathrm{Re} = 7812.5$, also a quaternary vortex begins to appear in the left lower corner.

7.4. Periodic Solutions

Several long-time simulations have been completed for $\mathrm{Re} > \mathrm{Re}_{\mathrm{cr}}$. In this case, the system evolves to an asymptotic solution which is a periodic oscillation. For all the Reynolds numbers in the range $8018.8 < \mathrm{Re} < 8750$, the solutions exhibit similar time evolutions. As shown in Fig. 9, after an initial transient ($t < 300$) the system seems to converge to an equilibrium with energy fluctuations weaker than 10^{-8}. This equilibrium is, however,

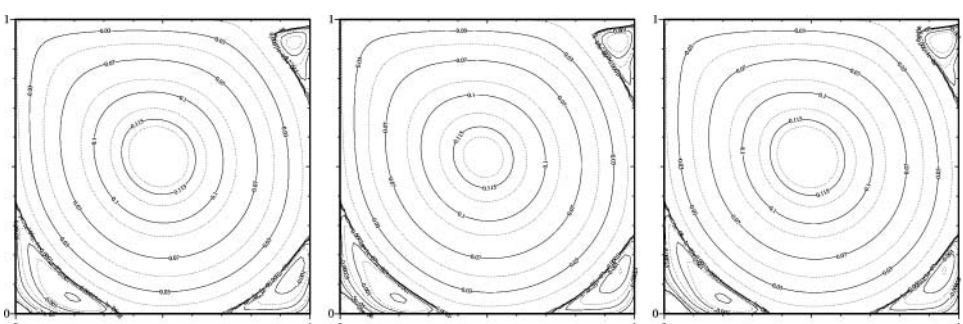

FIG. 8. Steady streamlines for $\mathrm{Re} = 6250$ (left), $\mathrm{Re} = 7500$ (middle), and $\mathrm{Re} = 7812.5$ (right).

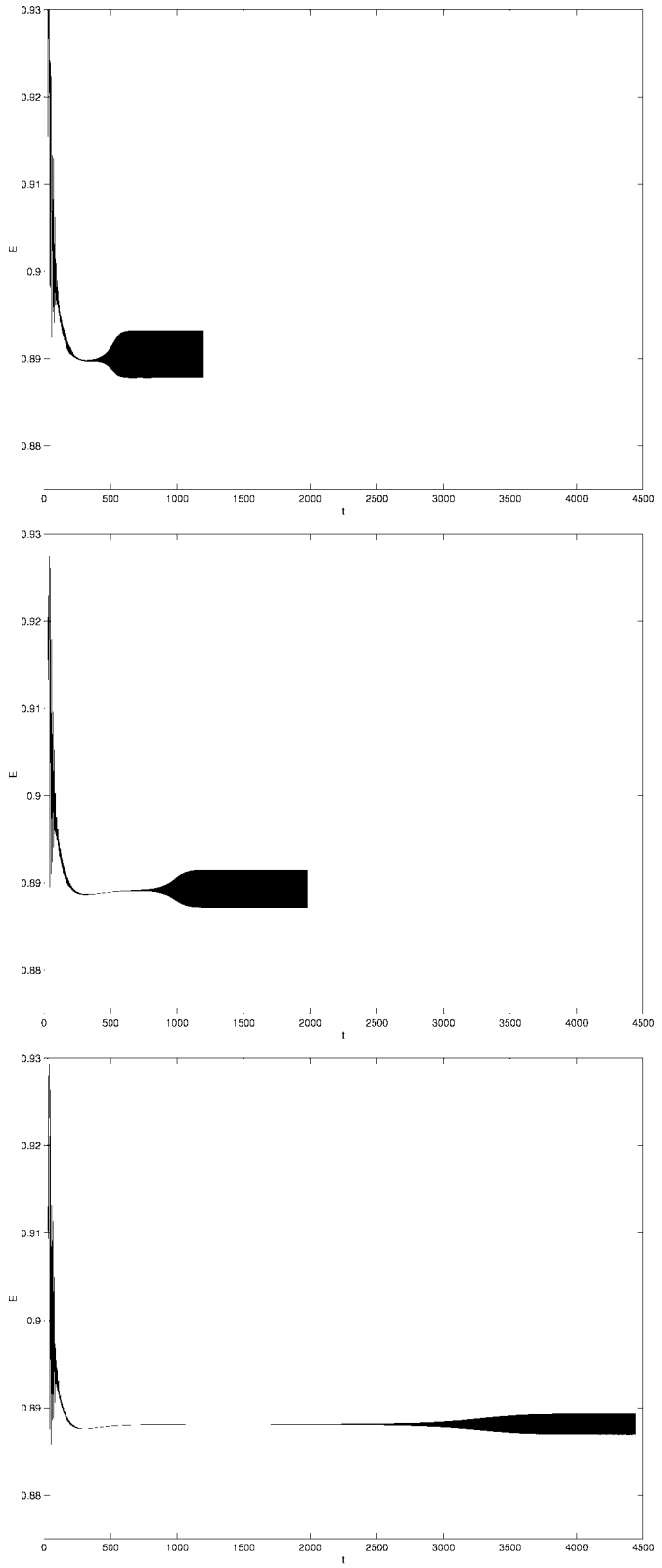

FIG. 9. Time evolution of the kinetic energy $E(t)$ for $\mathrm{Re} = 8750$ (top), $\mathrm{Re} = 8437$ (middle), and $\mathrm{Re} = 8125$ (bottom).

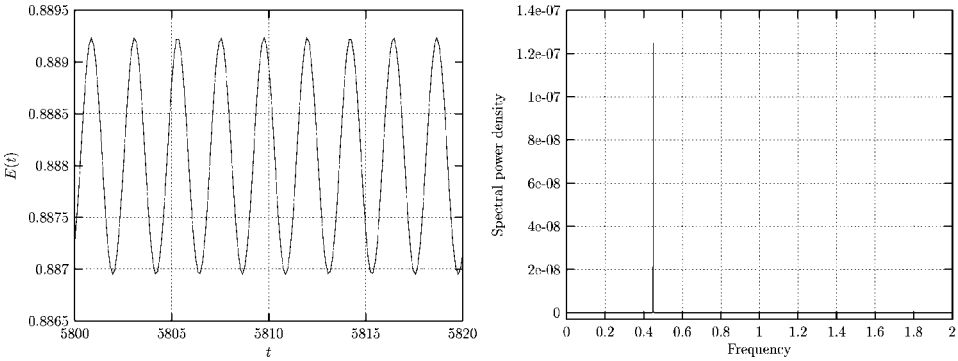

FIG. 10. Asymptotic time evolution (left) and spectral power density (right) of $E(t)$ for $\mathrm{Re} = 8125$.

unstable and for a time large enough the flow evolves toward a periodic solution with starting times and amplification rates which depend on $(\mathrm{Re} - \mathrm{Re}_{\mathrm{cr}})$.

This kind of time evolution is probably related to the presence of an unstable saddle equilibrium, generated by the loss of stability of the stable equilibrium.

The oscillatory asymptotic solution for $\mathrm{Re} = 8125$ is shown in the left plot of Fig. 10. The periodic character of the solution can be established by means of a Fourier analysis of $E(t)$. The right plot of Fig. 10 shows the spectral power density of $E(t)$ for $\mathrm{Re} = 8125$, obtained from a time series of 25,000 points over a time interval of size 3050.

The periodic solution can be represented also by its reconstruction in a bidimensional phase space. Figure 11 shows the phase portrait obtained using the delay coordinates $E(t)$ and $E(t + \tau)$ with $\tau = 0.735$.

The final periodic oscillation is found to have a fundamental frequency which depends linearly on Re, as shown by the left plot of Fig. 12 and as also observed by Shen in the case of the regularized cavity [28]. The linear behavior is, however, valid only up to the second bifurcation point, the location of which in Re will be described in the following. For $\mathrm{Re} = 8018.8$, the frequency is $f_1 = 0.4496$, a value very close to the one presented by Fortin *et al*. in [12], where $f = 0.4517$ for $\mathrm{Re} = 8000$. These values agree with the results

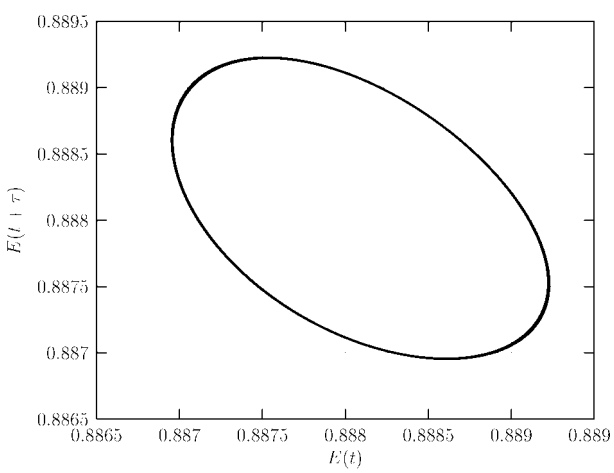

FIG. 11. Two-dimensional phase portrait of $E(t)$ for $\mathrm{Re} = 8125$, with $\tau = 0.735$.

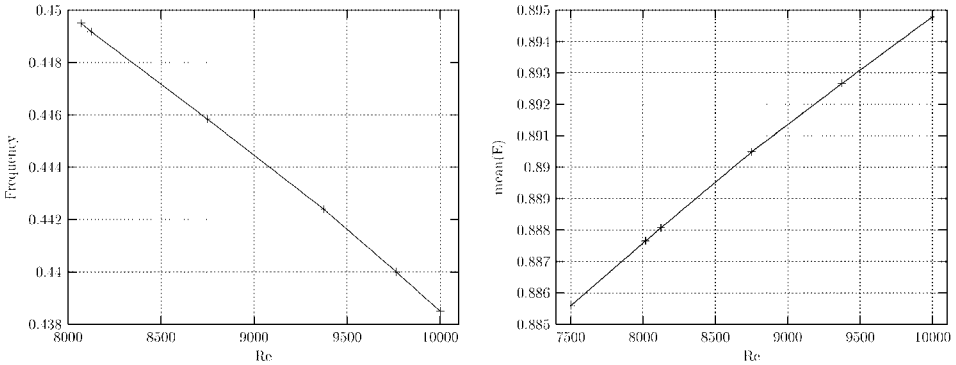

FIG. 12. Frequency (left) and amplitude (right) of energy oscillations for different Re.

of Pan and Glowinski [26]; for instance, at $\mathrm{Re} = 8500$ the present value $f = 0.447$ falls in the range $0.440 < f < 0.450$ reported by these authors. In contrast, the value of frequency $f = 0.4$ reported by Kupferman [22] for the same $\mathrm{Re} = 8500$ seems to be underestimated.

Similarly, the asymptotic mean value of $E(t)$ increases linearly with Re up to the second bifurcation, as shown by the right plot of Fig. 12, for $7500 \leq \mathrm{Re} \leq 10{,}000$.

Finally, as already noticed, the asymptotic amplitude of the oscillations depends on the closeness of Re to $\mathrm{Re}_{\mathrm{cr}}$; namely, for small supercritical values of the bifurcated solution the amplitude of the oscillation is $\mathcal{O}(|\mathrm{Re} - \mathrm{Re}_{\mathrm{cr}}|^{1/2})$ [12]. Figure 13 shows the oscillation amplitudes for the value of Re for which it has been possible to reach the asymptotic periodic solution. In the same figure we present the least-square interpolant of order $1/2$ based on the three points closest to $\mathrm{Re}_{\mathrm{cr}}$. This curve crosses the horizontal axis for $\mathrm{Re} \approx 8018$, further confirming the stability limit estimate.

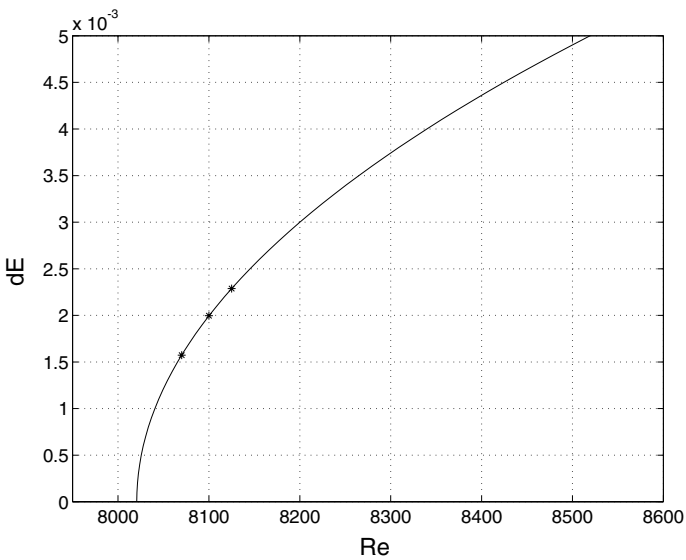

FIG. 13. Oscillation amplitude of $E(t)$ for different Re, dots represent values obtained from the simulation; the continuous line is the curve $\sqrt{\mathrm{Re} - \mathrm{Re}_{\mathrm{cr}}}$ obtained by least-square fitting of the points, with $\mathrm{Re}_{\mathrm{cr}} \approx 8018$.

7.5. Nature of the Periodic Solution

The analysis of the time series of the energy indicator allowed us to obtain an accurate estimate of the critical Reynolds number. On the other hand, this analysis does not supply any information about the fluid dynamic mechanism underlying the periodic behavior. For this purpose, a visualization approach can be pursued.

To characterize the oscillating component of the flow with $\mathrm{Re} > \mathrm{Re}_{cr}$, different techniques can be adopted. In [24], Le Quéré and Behnia visualize the fluctuating temperature fields of a differentially heated cavity by subtracting a time-averaged temperature field from each instantaneous temperature field. Similar results can be obtained by applying a bandpass filter to a series of fields of the considered variable. This second approach is found to be particularly useful when more than one frequency is present in the solution and we want to isolate the oscillation associated with only one.

In the present work, the time evolution of the vorticity field has been filtered by a bandpass filter in the range $0.42 \leq f \leq 0.48$ to display the fluctuating structures which take part in the periodic motion. In Fig. 14 we report a time series of nine fluctuating vorticity fields for $\mathrm{Re} = 8125$, separated by the time interval $T/9 = 1/(4f) = 0.247$, corresponding to a complete cycle.

The figure emphasizes the existence of an alternate vortex street which turns around the primary vortex. This vortex street consists of five structures, each presenting a couple of

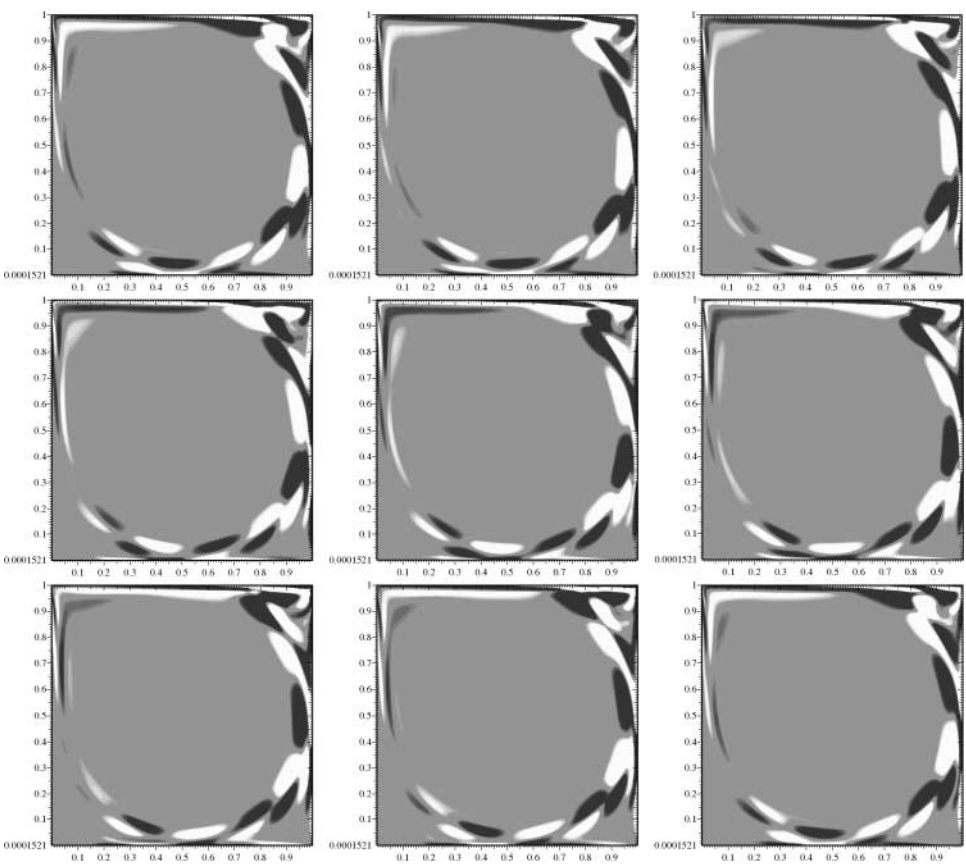

FIG. 14. Time sequence of fluctuating vorticity fields for $\mathrm{Re} = 8125$ obtained by means of a bandpass filter.

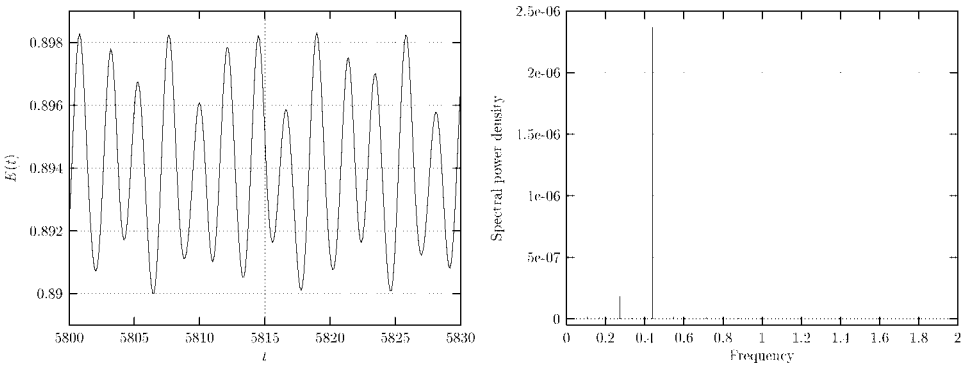

FIG. 15. Asymptotic time evolution (left) and spectral power density (right) of $E(t)$ for $\mathrm{Re} = 9765$.

adjacent vortices rotating with opposite spin. A similar behavior was described by Le Quéré *et al.* for the regularized cavity problem [23].

The formation of the vortex street (and consequently the periodic behavior of the system for $\mathrm{Re} > \mathrm{Re}_{\mathrm{cr}}$) seems to be due to the loss of stability of the shear layer which separates the primary vortex from the secondary vortex and the cavity walls.

7.6. Preliminary Analysis of the System beyond the First Bifurcation

Some preliminary investigations have been carried out on the behavior of the system beyond the first Hopf bifurcation. For $\mathrm{Re} = 9765$ a second incommensurate frequency $f_2 = 0.2736$ is found to be active. In Fig. 15 we present the asymptotic time evolution and the spectral power density of $E(t)$ for $\mathrm{Re} = 9765$.

In this case, the quasi-periodic behavior of the asymptotic solution for $\mathrm{Re} = 9765$ can be represented by the reconstruction of the attractor in a phase space with three dimensions. Figure 16 shows the two-dimensional torus corresponding to the quasi-periodic solution. The Poincaré section of this attractor is presented in Fig. 17.

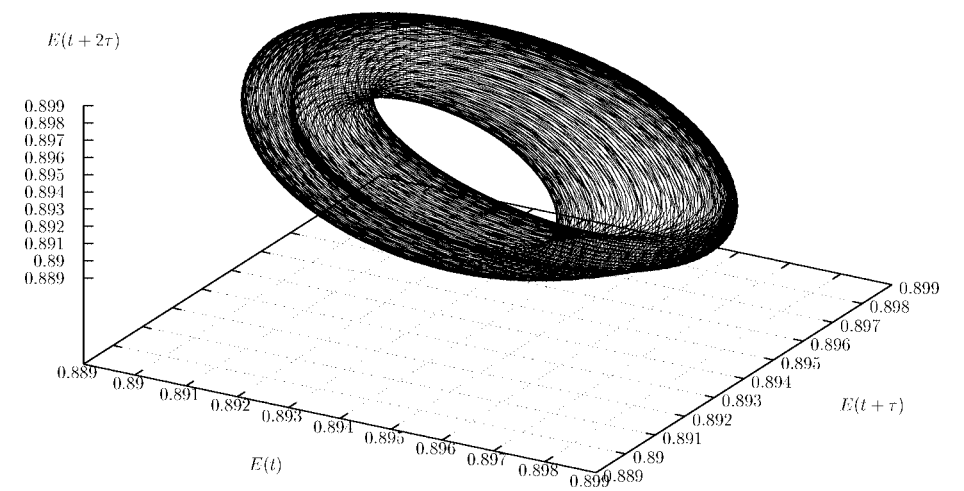

FIG. 16. Reconstruction in three-dimensional phase space of $E(t)$ for $\mathrm{Re} = 9765$, with $\tau = 0.7$.

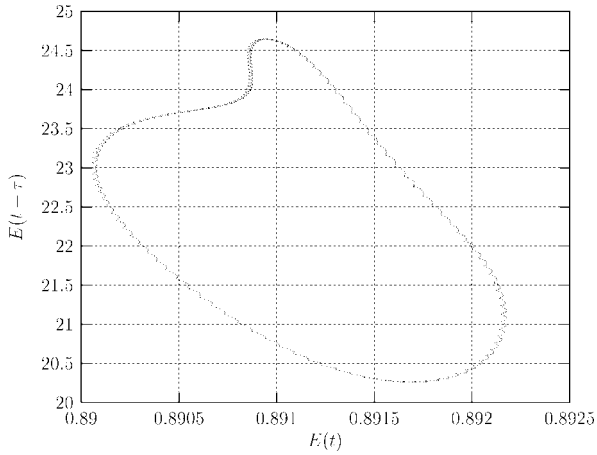

FIG. 17. The Poincaré section of the attractor for $\mathrm{Re} = 9765$, with $\tau = 0.7$.

This preliminary analysis beyond the first bifurcation led us to suppose that the system passes through a second Hopf bifurcation for a second critical Reynolds number located in the interval [9687, 9765).

8. CONCLUSIONS

In this paper, we presented a numerical investigation on the stability properties of the singular driven cavity problem. The dynamics of this system is analyzed by means of the time series of the kinetic energy obtained by the direct numerical simulation of the unsteady two-dimensional Navier–Stokes equations.

As a first result, we confirmed the existence of a Hopf bifurcation as the Reynolds number increases. By means of a bisection technique we were able to locate, for the first time, the critical Reynolds number in the narrow range [8017.6, 8018.8). These figures are quite near to the value obtained by Fortin *et al.* by means of an eigenvalue analysis based on a finite element spatial discretization. However, we claim better accuracy of our stability estimate for the singular driven cavity flow since the main singularities have been taken into account analytically.

Moreover, by analyzing the kinetic energy time series, we can formulate a hypothesis about the dynamical portrait of the system in the phase space. Indeed, before attaining its final asymptotic behavior, the solution seems to reach a steady state, with an oscillation amplitude as small as 10^{-8}—very small if compared with the oscillations in the initial transient, which have magnitude of $O(1)$. This behavior may be caused by the presence of a saddle equilibrium, which is probably generated by the splitting of a stable equilibrium for subcritical Reynolds numbers. This fact should be taken into account in selecting the stopping criteria in time-dependent simulations to avoid stopping before the true asymptotic solution has been achieved. Moreover, this unstable equilibrium could be one of the possible solutions obtained by steady solvers.

By visualizing the time evolution of the solution, cleaned of its steady component, we were able to get an insight into the fluid dynamic mechanism which generates the instability. Indeed, as the pictures in Fig. 14 show, the time-periodic solution is characterized by the presence of an alternate vortex street, arising from the loss of stability of the shear layer

which separates the main vortex from the secondary corner vortices and the cavity walls. The frequency and the amplitude of the periodic oscillations were found to depend on the value of Re, as predicted by the theory and as observed in the numerical simulation of the regularized cavity problem.

We would like to eventually emphasize the role played by the numerical technique in achieving the accuracy and efficiency required by this kind of investigations. Indeed these two goals, namely efficiency and accuracy, drove us to develop the proposed Galerkin–Legendre spectral solver for the solution of the time-dependent Navier–Stokes equations in two dimensions. By discretizing the problem in time by means of the BDF incremental projection method we obtained the time accuracy and efficiency needed by the long simulations to be performed in this kind of stability analysis. Moreover, the singularity subtraction technique, as proposed by Botella and Peyret, has been extended here to the time-dependent Navier–Stokes equations to avoid the pollution of the transient solutions by Gibbs oscillations due to the singular nature of the problem, and very accurate results have been obtained even by a spectral method, which is generally unsuitable for low regularity problems.

REFERENCES

1. F. Auteri, J.-L. Guermond, and N. Parolini, Role of LBB condition in weak spectral projection methods, *J. Comput. Phys.* **174**, 405 (2001).
2. F. Auteri and N. Parolini, A mixed-basis spectral projection method, *J. Comput. Phys.* **175**, 1 (2002).
3. F. Auteri and L. Quartapelle, Galerkin spectral method for the vorticity and stream function equations, *J. Comput. Phys.* **149**, 306 (1999).
4. F. Auteri, L. Quartapelle, and L. Vigevano, Accurate ω–ψ spectral solution of the singular driven cavity problem, *J. Comput. Phys.* **180**, 597 (2002).
5. G. Batchelor, *An Introduction to Fluid Dynamics* (Cambridge Univ. Press, Cambridge, UK, 1967).
6. B. J. Bayly, S. A. Orszag, and T. Herbert, Instability mechanisms in shear-flow transition, *Ann. Rev. Fluid Mech.* **20**, 359 (1988).
7. C. Bernardi and Y. Maday, *Approximations spectrales des problèmes aux limites elliptiques* (Springer-Verlag, Paris, 1992).
8. O. Botella and R. Peyret, Benchmark spectral results on the lid-driven cavity flow, *Comput. Fluids* **27**, 421 (1998).
9. O. Botella and R. Peyret, Computing singular solutions of the Navier–Stokes equations with the Chebyshev collocation method, *Int. J. Numer. Methods Fluids* **36**, 125 (2001).
10. S. Chandrasekhar, *Hydrodynamic and Hydromagnetic Stability* (Clarendon, Oxford, 1961).
11. P. G. Drazin and W. H. Reid, *Hydrodynamic Stability* (Cambridge Univ. Press, Cambridge, UK, 1981).
12. A. Fortin, M. Jardak, J. Gervais, and R. Pierre, Localization of Hopf bifurcation in fluid flow problems, *Int. J. Numer. Methods Fluids* **24**, 1185 (1997).
13. U. Ghia, K. N. Ghia, and C. T. Shin, High-Re solutions for incompressible flow using the Navier–Stokes equations and a multigrid method, *J. Comput. Phys.* **48**, 387 (1982).
14. R. Glowinski, H. B. Keller, and L. Reinhart, Continuation-conjugate gradient methods for the least square solution of nonlinear boundary value problems, *SIAM J. Sci. Stat. Comput.* **6**, 793 (1985).
15. J. W. Goodrich, K. Gustafson, and K. Halasi, Hopf bifurcation in the driven cavity, *J. Comput. Phys.* **90**, 219 (1990).
16. J.-L. Guermond, Un résultat de convergence à l'ordre deux en temps pour l'approximation des équations de Navier–Stokes par une technique de projection, *Modél. Math. Anal. Numér.* **33**, 169 (1999).
17. M. M. Gupta, R. P. Manohar, and B. Noble, Nature of viscous flows near sharp corners, *Comput. Fluids* **9**, 379 (1981).

18. K. Gustafson and K. Halasi, Vortex dynamics of cavity flows, *J. Comput. Phys.* **64**, 279 (1986).
19. K. Gustafson and K. Halasi, Cavity flow dynamics at higher Reynolds number and higher aspect ratio, *J. Comput. Phys.* **70**, 271 (1987).
20. C. Hancock, E. Lewis, and H. K. Moffatt, Effects of inertia in forced corner flows, *J. Fluid Mech.* **112**, 315 (1981).
21. M. Kawaguti, Numerical solution of the Navier–Stokes equations for the flow in a two dimensional cavity, *J. Phys. Soc. Jpn.* **16**, 2307 (1961).
22. R. Kupferman, A central-difference scheme for a pure stream function formulation of incompressible viscous flows, *SIAM J. Sci. Comput.* **23**, 1 (2001).
23. P. Le Quéré, A. Dalieu, and Ta Phouc Loc, *Investigation of 2-D and 3-D Instability of the Driven Cavity Flow*, LIMSI-CNRS, BP 133, 91403 Orsay Cedex, France.
24. P. Le Quéré and M. Behnia, From onset of unsteadiness to chaos in a differentially heated square cavity, *J. Fluid Mech.* **359**, 81 (1998).
25. S. A. Orszag, Numerical simulation of incompressible flows within simple boundaries: I. Galerkin (spectral) representation, *Stud. Appl. Math.* **50**, 293 (1971).
26. T. W. Pan and R. Glowinski, A projection/wave-like equation method for the numerical simulation of incompressible viscous fluid flow modelled by the Navier–Stokes equations, *Comput. Fluid Dyn. J.* **9**, 28–42 (2000).
27. N. Ramanan and G. M. Homsy, Linear stability of the lid-driven cavity flow, *Phys. Fluid* **6**, 2690 (1994).
28. J. Shen, Hopf bifurcation of the unsteady regularized driven cavity, *J. Comput. Phys.* **95**, 228 (1991).
29. J. Shen, Efficient spectral-Galerkin method. I. Direct solvers of second- and fourth-order equations using Legendre polynomials, *SIAM J. Sci. Comput.* **15**, 1489 (1994).
30. R. Schreiber and H. Keller, Driven cavity flows by efficient numerical techniques, *J. Comput. Phys.* **49**, 310 (1983).
31. W. W. Schultz, N. Y. Lee, and J. P. Boyd, Chebyshev pseudospectral method of viscous flows with corner singularities, *J. Sci. Comput.* **4**, 1 (1989).